CHINA FOUNDRY Research & Development
Vol. 22 No. 5 September 2025
www.springer.com/41230
https://doi.org/10.1007/s41230-025-4021-5

Effects of infill patterns on properties of slurry extrusion-based additive manufactured shell moulds

Jiao Liu, *Hong-jun Liu, Guo-liang Su, and Ya-min Li

State Key Laboratory of Advanced Processing and Recycling of Non-ferrous Metals, Lanzhou University of Technology, Lanzhou 730050, China

Abstract: Investment casting shell moulds are widely applied to cast alloys, but how to efficiently form a hierarchical porous structure inside the wall is an innovation and challenge. In this research, porous shell moulds with three infill patterns (rectilinear, grid, and honeycomb) were prepared using bauxite slurry and slurry extrusion-based additive manufacturing technology, and the effects of infill patterns on the properties were evaluated. The hierarchical pores inside the wall are composed of the macropores formed by infills and the micropores among bauxite particles. Different infill patterns result in changes in distribution and shape of pores, thereby affecting the properties of the shell moulds. The honeycomb pattern has more comprehensive advantages compared to the other two infill patterns. The samples prepared with the honeycomb pattern exhibit the highest bending strength (11.62 MPa) and porosity (41.6%), as well as good heat-transfer ability, with an average shrinkage rate within 2.0%. This work provides an attractive feasibility for fabricating shell moulds with hierarchical porous walls.

Keywords: additive manufacturing; slurry extrusion; infill pattern; casting shell mould; bauxite; investment casting

CLC numbers: TG221 **Document code:** A **Article ID:** 1672-6421(2025)05-574-09

1 Introduction

Additive manufacturing (AM) is a revolutionary manufacturing technology that integrates digitalization, intelligence and environmental friendliness and can directly fabricate shell moulds for the investment casting process without wax patterns [1-4]. The AM technologies of the casting shell moulds have the advantages of reduced manufacturing lead time, shortened process, low cost, and high flexibility [5,6]. Currently, AM processes that can be used to fabricate casting shell moulds mainly include stereolithography (SLA), selective laser sintering (SLS), binder jetting, and slurry extrusion-based additive manufacturing. Chen et al. [7] prepared alumina moulds using SLA and investigated the effects of particle size distribution and sintering temperature on the properties, and the results showed the sample possessed relatively low sintering shrinkage, proper mechanical strength, porosity, and high-temperature properties that meet the requirements for casting purposes. Gu et al. [8] fabricated Al_2O_3 ceramic cores with fine complex geometric shapes by SLA, and the flexure strength and open porosity of ceramic cores were supposed to meet the requirement of ceramic cores for the fabrication of superalloy blades. A novel binder-coated Al_2O_3 sand for SLS was developed to manufacture complex sand moulds for metal casting, which shortened the trial production cycle of the six-cylinder engine from five months of the traditional casting method to 10 days [9]. The mullite ceramic shell moulds could be fabricated by SLS combined with the high-temperature sintering process, and their mechanical properties far exceeded those of shell moulds fabricated by the traditional shell-making process [10]. Based on the binder jetting process, a shell mould with a thickness of 10 mm was manufactured using hemihydrate calcium sulphate as the powder material and 2-pyrrolidone as the binder, indicating that it has the advantage of creating sand moulds with less time and much more complex geometries [11]. Another material composed of furan resin and silica sand was also used to prepare sand moulds using the binder jetting process. It was found that the three-point bending strength of 3D printed sand mould

*Hong-jun Liu

Male, born in 1974, Ph. D., Professor. His research interests mainly focus on the slurry extrusion-based additive manufacturing, rapid casting, advanced metal composite materials, and precision casting technologies.

E-mail: hongjun_liu@hotmail.com

Received: 2024-02-02; Revised: 2024-07-07; Accepted: 2024-11-07

attained its maximum when cured at 100 °C for 2 h, regardless of the binder content [12].

The slurry extrusion-based additive manufacturing is an AM process based on the principle of direct ink writing [13-16]. It uses high solid loading ceramic slurry with shear thinning characteristics, and the filaments formed by the extrusion of ceramic slurry are stacked layer by layer on the building platform to form moulds. The slurry can be accurately deposited at preset positions, providing a AM method for complex structures such as unsupported suspension or hollow wall with network infills [17, 18]. This process has advantages such as wide adaptability, flexible process, simple equipment, and short production cycle. The investigation of extrusion-based additive manufacturing of Y_2O_3-based ceramic shell moulds found that small amounts of $CaTiO_3$ can reduce sintering temperature and significantly increase bending strength [19]. Choi et al. [20] proposed a new extrusion-based additive manufacturing process combined with an organic-inorganic binder conversion process to fabricate a ceramic core with high dimensional stability. Xing et al. [21] proposed a structural analysis algorithm for shell-like models for ceramic materials and presented a computational framework to enhance the structural stability. The experimental results for Al_2O_3 refractory products showed that layer height was an effective parameter for tuning the inter-space size and the adhesion between layers [22].

In addition to materials and processes, the infills are also an important factor affecting the properties of parts prepared with the extrusion-based additive manufacturing process [23, 24]. The infills provide stable and sturdy structural support for the appearance and properties. Fused deposition manufacturing (FDM) is the most typical extrusion-based additive manufacturing process. The acrylonitrile-butadiene-styrene (ABS) samples with different infill patterns and infill densities were manufactured using FDM and the strength test results showed that the influence of the different printing patterns caused a variation of less than 5% in infill density and the change in infill density mainly determined the tensile strength [25]. Another study on the synergistic effects of different infill patterns and infill densities with varying thicknesses of layers on ABS samples revealed that the infill pattern greatly affected both tensile and impact strengths [26]. Through the comparative study of finite element analysis and physical experimentation on polylactic acid (PLA) samples, the mechanical properties of samples with different lattice topologies showed that vin tile cellular structure bears less stress and the lowest deformation [27]. Man et al. [28] investigated the effects of topological structures on the mechanical properties of the hollow load bearing boards prepared from the slurry of kaolin clay and alpha-Al_2O_3 powder and proved that the honeycomb grid was the most appropriate structure. The hollow ceramic cores with lattice structures prepared by SLA proved that the lattice structure improved the core-removal efficiency by over three times [29].

A hollow wall with an internal porous structure can provide lightweight and material-saving benefits for the casting shell mould. However, when preparing the shell mould with a hollow wall using AM processes such as SLA, SLS, and binder jetting, their manufacturing characteristics determine the inevitable presence of unstructured excess materials in the internal structure of the wall. Therefore, for internally hollow structures, it is necessary to reserve openings to facilitate the removal of unstructured excess materials [1, 29-32]. The slurry extrusion-based additive manufacturing process does not have such limitations. The hollow wall with internal controllable porous structure can be directly prepared by setting the "infill" parameter in slicing software, and there will be no unstructured materials inside the hollow wall during the manufacturing process. Our research team previously investigated the influence of wall structure (wall thickness, wall height, and infill pattern) on the dimensional accuracy of shell moulds, with findings demonstrating the significant impact of infill patternson the dimensional accuracy [33]. In this study, the effect of infill patterns on the properties of shell moulds was further investigated. The shell mould with hollow walls was designed and prepared using slurry extrusion-based additive manufacturing. The effect of different infill patterns on the properties of shell mould was evaluated. Furthermore, a trial casting was carried out to verify the feasibility of the shell mould with a novel structure for casting.

2 Experimental

2.1 Slurry preparation

The slurry was prepared with bauxite as refractory powder and silica sol as the binder. The nominal particle size of bauxite powder was 15 μm, and the SiO_2 content of silica sol was 30wt.%. The contents of bauxite and silica sol in the slurry were 66.0wt.% and 26.5wt.%, respectively. Other ingredients included sodium polycarboxylate (3.5wt.%), glycerol (3.0wt.%), and PEG400 (1.0wt.%). The mixture of silica sol, sodium polycarboxylate, glycerol, and PEG400 was prepared by magnetic stirring for 10 min. Then, the bauxite powder was added to the mixture to ball mill at 50 r·min^{-1} for 40 min to achieve a good dispersion. Finally, the viscosity of the slurry was adjusted with the acid thickener. The steady-state shear viscosity of the slurry used for extrusion is shown in Fig. 1, which was measured with a viscometer (NDJ-8S, Fangrui, China). The slurry shows good shear thinning characteristics.

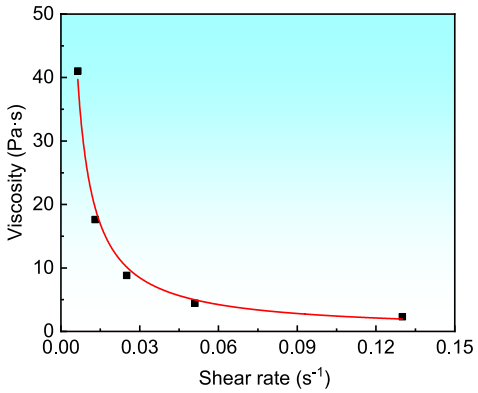

Fig. 1: Steady-state shear viscosity of slurry

2.2 Additive manufacturing and subsequent processing

The additive manufacturing process of the shell mould was performed by extrusion-based equipment with the delta mechanism and screw extruder, as shown in Fig. 2. The feeding system was a mechanically driven plunger type. The CAD models were designed and then output as the STL files. The G codes were generated after slicing according to the layer thickness. The slurry was loaded into the barrel and fed to a screw extruder driven by a motor. The nozzle moved along the printing paths to stack the extruded filaments layer by layer to form the green parts. The nozzle movement speed was 20 mm·s^{-1}, and the extrusion rate was set to multiplier 1.0 (the feeding amount of the slurry and theoretical deposition volume of filaments were equal).

The green parts were first freeze-dried in a vacuum freeze-dryer for 24 h, then, placed into a muffle furnace and heated to 1,100 °C at a rate of 10 °C·min^{-1}. After being sintered at 1,100 °C for 4 h and cooled to room temperature naturally, the shell moulds were ready for testing and casting. Due to the very low organic content in the materials, the preparation of the shell mould did not require a specific debinding process.

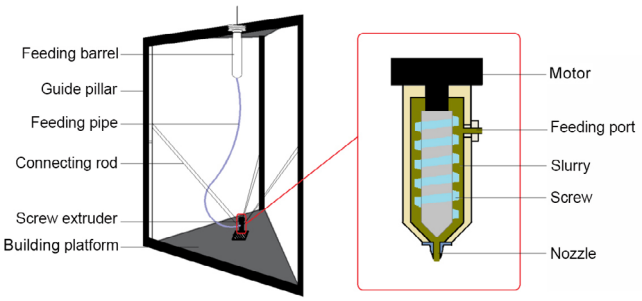

Fig. 2: Schematic diagram of extrusion-based additive manufacturing equipment

2.3 Design of infill patterns

In this study, a nozzle with a diameter of 1.2 mm was used, and the layer height was set to 0.96 mm (80% of the nozzle diameter). If the layer height is set too low, the extruded slurry will exert significant pressure on the previous layer and is prone to randomly overflowing out of the contour, resulting in poor accuracy and increased possibility of collapse. If the layer height is set too high, both the interfacial contact area between newly extruded filament and previously deposited layer, and the dynamic pressure exerted by the extruded slurry will decrease. This results in weakened interlayer bonding. When the interlayer bonding strength is too low, interlayer cracking may occur during the sintering process. After preliminary experiments, a layer height of 0.96 mm can achieve high forming accuracy while ensuring better interlayer bonding effect.

A comparative study was performed on three infill patterns: rectilinear, grid, and honeycomb, as shown in Fig. 3. In this experiment, the outline layer was first filled, and then the infill was filled. The infill percentage was set to 80% and the infill angle was set to 45°. The rectilinear pattern had a structure with two sets of parallel lines that were filled alternately every two layers and orthogonal to each other. The grid pattern orthogonally filled two sets of parallel lines in one layer. A set of parallel lines was first filled, and then another set of parallel lines orthogonal to the previous set of lines was filled in the same layer. Similar to the rectilinear pattern, the structure of the honeycomb pattern was also repeated every two layers, but its path was a combination of line segments with a angle of 120°.

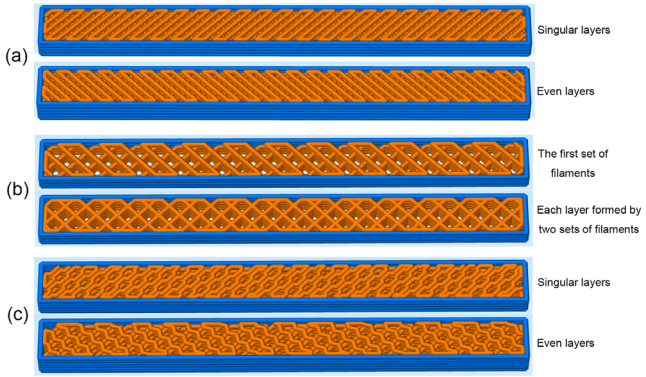

Fig. 3: Structural diagram of infill patterns: (a) rectilinear; (b) grid; (c) honeycomb

2.4 Characterization

The surface morphology and microstructure were observed using scanning electron microscopy (SEM, Sigma300, ZEISS, Germany). The three-point flexural strength was measured by a computerized electronic universal testing machine (WDW-100D, Suns, China), which was performed under working parameters of 60 mm span and a loading rate of 0.5 mm·min^{-1}. The sample size was 100 mm×10 mm×10 mm. For each infill pattern, five samples were measured and the average value was calculated. The heat-transfer ability of the shell mould was measured, as shown in Fig. 4. Two K-type thermocouples were respectively placed inner and outer sides of a 5 mm-thick shell mould wall. After pouring A356 aluminum alloy melt, the temperature was recorded using a data acquisition instrument and the temperature difference between the two thermocouples was calculated.

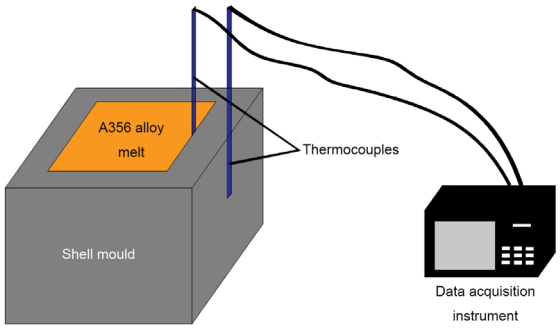

Fig. 4: Schematic diagram of heat-transfer ability measurement

Linear shrinkage, L, was calculated according to Eq. (1):

$$L = (l_1 - l_2) / l_1 \quad (1)$$

where, l_1 is the dimension of the freeze-dried sample, and l_2 is the dimension of sintered sample.

For each infill pattern, three samples with the size of 60 mm×10 mm×6 mm were prepared and the measurement was the average of dimensions of three positions. The structure size of the sample shows significant differences in the building plane (X-Y plane) and height direction (Z direction), therefore, the shrinkage in different directions needs to be separately measured. The size of the sample in the Y direction was small and the internal periodic structures were limited, so the shrinkage of the sample in the X direction was selected to evaluate its shrinkage on the building plane. The X, Y, and Z directions of the sample are shown in Fig. 5.

Archimedes' method was used to measure the open porosity of sintered sample, P, which was calculated by Eq. (2). The measured porosity is the sum of macroscopic and microscopic pores.

$$P = (m_2 - m_1)/(m_2 - m_3) \quad (2)$$

where, m_1 is the mass of the sintered sample, m_2 and m_3 are the weight of water-saturated sample in water and air, respectively.

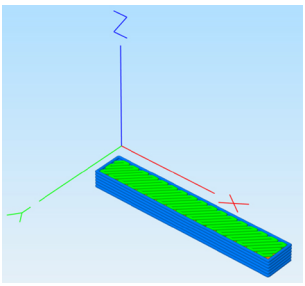

Fig. 5: Measurement directions of linear shrinkage

3 Results and discussion

3.1 Appearance and microstructure

To examine the formability of the walls of shell moulds with different infill patterns and their robustness under high-temperature processing, the appearance was compared for the three-point flexural strength samples before and after sintering. As shown in Fig. 6, the samples exhibit no discernible deformation or macrocracks, while the extruded filaments demonstrate excellent continuity and uniformity. The layered features on the samples' lateral surfaces are distinct, forming a rough surface texture. Although the samples has different internal structures, their design structures of outermost layer are identical, no discernible difference in the appearance. Notably, the sintering conditions for all samples are identical, and the bonding characteristics of bauxite powder are solely determined by the sintering process, so the internal filling structures at the millimeter scale can not affect the interparticle microstructure at the micrometer scale. Consequently, in the SEM observations presented in Fig. 7, the sample with rectilinear infill pattern was selected as a representative example to demonstrate the surface morphology and microstructure before and after the sintering process.

In Figs. 7(a) and (c), the microcracks can be observed on the surface, especially at the intersection of filaments, which can be attributed to shrinkage during freeze-drying and sintering. Notably, compared with the samples before sintering, the samples after sintering show fewer microcracks, as sintering promotes the connections among particles and causes shrinkage. As shown in Figs. 7(b) and (d), the microstructure of the extruded filaments in samples is composed of bauxite particles and interconnected micropores, which do not shows significant changes before and after sintering. The macropores formed through infills (Fig. 3) and the micropores among

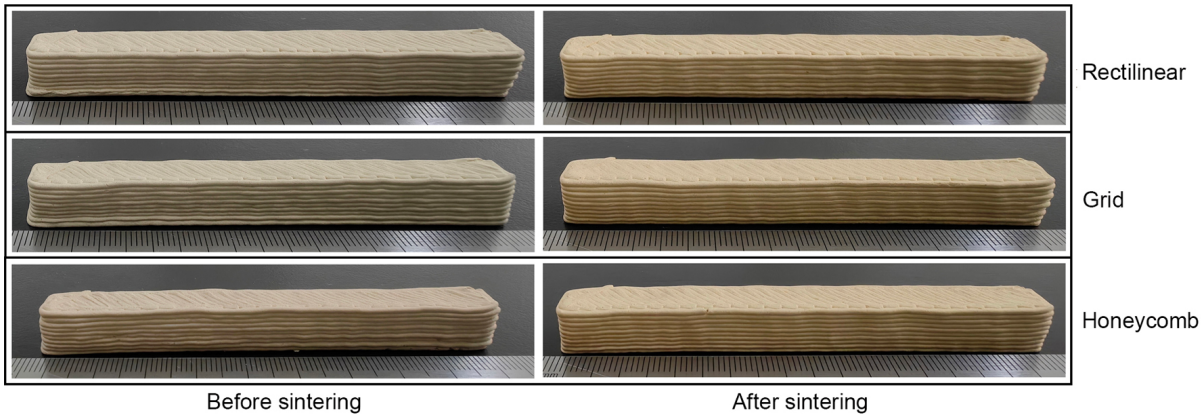

Fig. 6: Appearance of samples with different infill patterns

particles [Fig. 7(d)] construct a hierarchical porous structure in walls. This is the characteristic of shell moulds prepared by the additive manufacturing technology, which is significantly different from traditional shell moulds of investment casting that only have micropores among refractory particles.

3.2 Flexural strength

The shell moulds should have enough flexural strength to avoid deformation, cracks, and damage under complex stress during handling, pouring, and other processes. The flexural strength of shell moulds for investment casting is generally

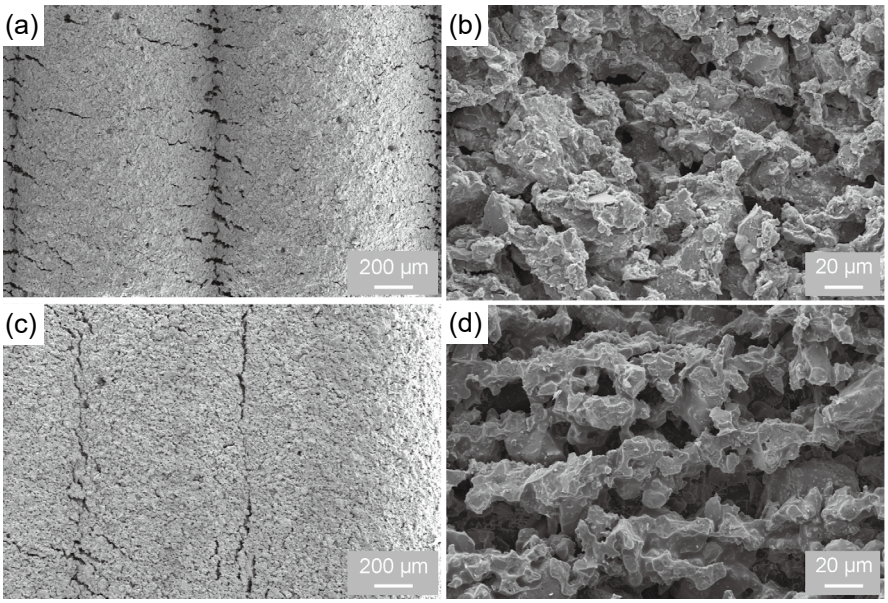

Fig. 7: SEM micrographs of surface and fracture microstructure of samples with rectilinear infill pattern: (a, b) before sintering; (c, d) after sintering

not less than 4.0 MPa [34-37]. In Fig. 8(a), the flexural strength of all samples with three various infill patterns is greater than 9 MPa. The average strength of samples with honeycomb pattern is the highest, which is 19.3% higher than that with rectilinear pattern and 17% higher than that with grid pattern. The strength of the sample mainly comes from the formation of the mullite phase after high-temperature sintering of bauxite and the crystallization transformation of silicate gel after dehydration of silica sol [38]. As shown in Fig. 7(d), the bauxite particles come into contact with each other and fuse together at high temperatures, resulting in tight connections of filaments and layers. For rectilinear pattern and gird pattern, the filling paths are straight line and the contacts of filaments between layers are in the same position. While the hexagonal filling path of honeycomb pattern forms a larger contact area and more particle connection points, and the contact positions are more dispersed. As a result, samples with honeycomb pattern have the strongest resistance to bending deformation and the highest average flexural strength.

Figure 8(b) shows typical applied stress-deflection curves, which represent the resistance behavior to flexural deformation. The curves for the three infill patterns are very similar. As the deflection increases, the stress gradually increases in the initial stage, then presents a plateau region in the middle stage, and increases rapidly until the sample fractures in the final stage. When the flexural deformation of the sample is relatively small, no fracture occurs within the internal structure, and the deformation follows the law of elastic deformation. Due to the complexity of the hierarchical porous structure, the stress increases nonlinearly with deflection. When the flexural deformation is large enough, the network structure of infills inside the sample begins to fracture. The fracture of infills is gradually propagated from the midpoint with the maximum deformation to both sides. In the fracture propagation stage, the stress is nearly unchanged with deflection, resulting the plateau region. In the last stage, the deflection continues to increase, and the outer layers bear almost all of the deformation resistance. The integrity of the outer layers means that fracture requires greater external force, and sample undergoes disintegration as the outer layers fracture. Therefore, the stress values of the plateau region for different infill patterns are almost the same. However,

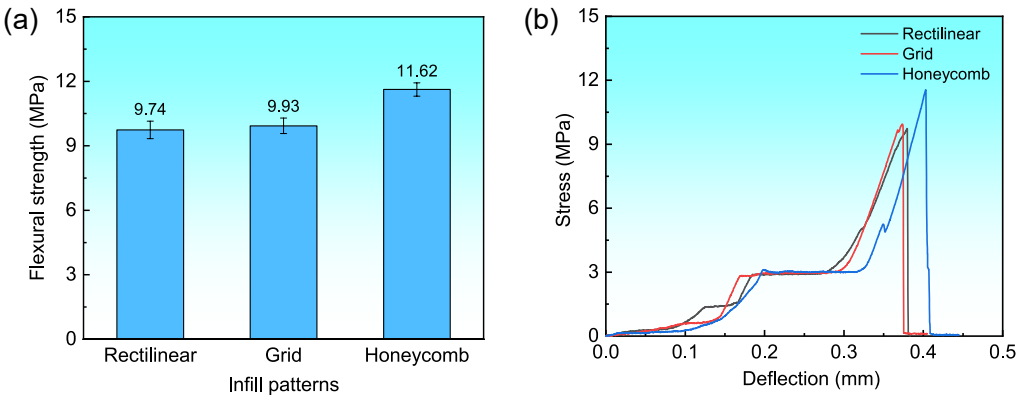

Fig. 8: Flexural strength testing results: (a) flexural strength; (b) stress-deflection curves

the flexural strength values reflect the disintegration of the samples, and vary for different infill patterns. The maximal difference in average flexural strength reaches 1.88 MPa.

The filling paths for rectilinear and grid patterns are straight lines, while those for honeycomb pattern consist of multiple line segments with a angle of 120° (Fig. 3). Therefore, when the sample undergoes a flexural deformation, the polygonal line path provides greater buffering than the straight line path. The sample with honeycomb pattern produces more significant deformation than the samples with the other two patterns. Moreover, the honeycomb infill exhibits higher deformation energy consumption, which can provide stronger support for the outer layers. As a result, the sample with honeycomb pattern exhibits greater deflection and higher flexural strength.

3.3 Porosity and shrinkage

The total porosity for sintered samples with three different infill patterns is shown in Fig. 9(a). The porosity is the highest for honeycomb pattern, followed by rectilinear pattern, and the sample with the grid pattern has the lowest porosity. It should be noted that the porosity is composed of both the macropores in the internal filling network structure of infills and the micropores among bauxite particles. According to the preset infill density of 80%, theoretical porosity of macropores should be 20%. The measured porosity is significantly higher than 20%, which is mainly attributed to the increase in total porosity by micropores [Fig. 7(d)]. Other factors that may bring about changes in porosity include the actual diameter of the extruded filaments, the overlapping between layers and the connections between infills and outer layers. For rectilinear and honeycomb patterns, the extruded filaments in different layers are in point contact, while for the grid pattern, they are in line contact, which leads to the main difference in porosity. Overall, the sample with the honeycomb pattern has a higher porosity, indicating that the shell moulds have the characteristics of lightweight and high air permeability, which is beneficial for high-quality castings.

Comparing Fig. 8(a) and Fig. 9(a), it can be seen that there is no corresponding relationship between porosity and flexural strength, which is different from traditional casting shell mould. Because the additive manufactured shell moulds are hierarchical porous structure with heterogeneous material distribution inside, their strength is mainly determined by the internal network structure of infills rather than the volume of pores. This result further indicates the advantages of slurry extrusion-based additive manufactured shell moulds: by optimizing the infill structure, the porosity and permeability can be improved without reducing strength.

During sintering, the shell moulds unavoidably undergo shrinkage, and due to the anisotropy of the structure, the shrinkage in various directions may be different. Figure 9(b) shows the shrinkage of the samples in *X* and *Z* directions. The samples with the grid pattern and honeycomb pattern undergo similar average sintering shrinkage. The difference values in shrinkage in *X* and *Z* directions are very small, only about 0.2%, which can be generally considered as isotropic shrinkage. The samples with rectilinear pattern have the lowest shrinkage, with a *Z*-direction shrinkage as low as 0.46%. However, the anisotropy of shrinkage is significant, and the difference in shrinkage in the *X* and *Z* directions can reach 1%.

The shrinkage in *X* direction is greater than that in *Z* direction, which is attributed to the fact that the porousness on the building plane is more pronounced than that in the height direction. The difference in shrinkage for different infill patterns is due to the different resistances of the internal network structure to the sintering shrinkage. As shown in Fig. 3, the rectilinear pattern has the finest porous network structure, resulting in effective dispersion of sintering shrinkage and the lowest shrinkage. Although the porous network structure of the honeycomb pattern is finer than that of the grid structure, its hexagonal network structure has weaker resistance to shrinkage of outer layers compared to the linear network structure of the grid pattern, resulting in similar shrinkage for both structures. In *Z* direction, the contact mode of extruded filaments between adjacent layers is the main factor responsible for variations in shrinkage. For the rectilinear pattern, the filaments in each layer are stacked perpendicular to that in the previous layer, and the filaments between adjacent layers are in point contact. The grid pattern is linear contact, while the honeycomb pattern is a mixture of point contact and line contact. As a result, the shrinkage in *Z* direction is the lowest for rectilinear pattern. Although the shrinkage of the sample with rectilinear pattern is the lowest, the significant anisotropy shrinkage is not conducive to accuracy control up to a point.

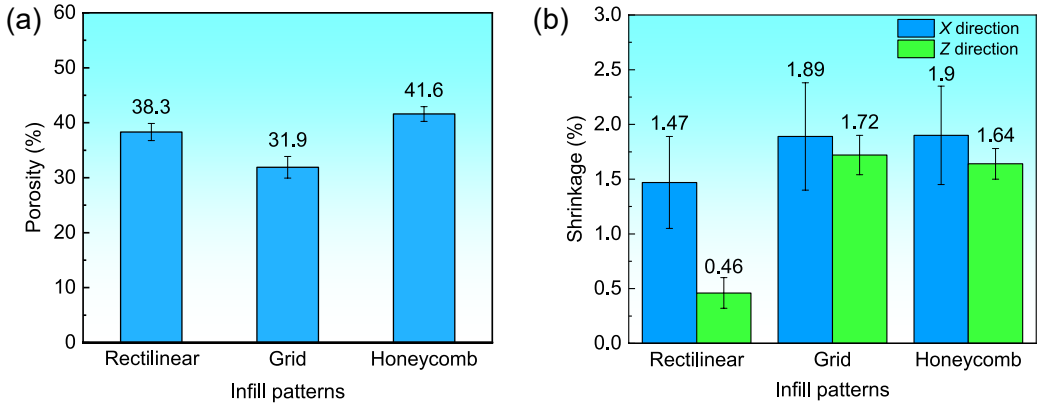

Fig. 9: Porosity and shrinkage of sintered samples: (a) porosity; (b) shrinkage

3.4 Heat-transfer ability

The different internal structures of walls with three various infill patterns affect the heat-transfer ability of the shell moulds. After pouring the alloy melt, the temperature difference inside and outside the shell moulds will be different. The temperature difference test results of samples with different infill patterns are shown in Fig. 10. The actual recorded highest temperature is lower than 600 °C, while the pouring temperature of A356 aluminum alloy is 720 °C, which is due to the cooling effect of the armored thermocouple and the shell mould.

The temperature curves show a similar trend, with the temperature rapidly reaching its maximum value and then slowly decreasing. Therefore, after the alloy melt is poured, the heat transfer through the wall can be divided into two stages. In the first stage, the innermost layer of the wall quickly reaches its maximum temperature, but the outermost layer takes 2–3 min to reach its maximum temperature. The bauxite skeleton undergoes a temperature rise process, and the air in the macropores and micropores is heated and expanded. The second stage of heat transfer is from the moment the wall reaches its maximum temperature until the casting cools down, and the shell mould gradually dissipates heat. The bauxite skeleton and the air in pores gradually decrease in temperature and undergo volume shrinkage. The heat transfer of shell mould is a combination of the conduction through bauxite skeleton and the convection of air in internal pores. In the first stage, the shell mould is mainly subjected to be heated, while in the second stage, the shell mould undergoes a cooling process.

Figure 10 indicates that the temperatures inside the shell moulds with rectilinear, grid, and honeycomb patterns reach up to 583 °C, 590 °C, and 586 °C, respectively, with little differences. While, the maximum temperatures outside the shell moulds are 273 °C, 318 °C, and 342 °C, respectively, with significant differences. Therefore, in the first stage, the heat-transfer ability of the shell moulds with three infill patterns, from high to low, is honeycomb, grid, and rectilinear. As shown in Fig. 10(d), it is obvious that in the short period after pouring (about 3 min in this study), the greatest temperature difference between the inside and outside surfaces of the wall can be observed for rectilinear pattern. The reason is that the rectilinear pattern forms much finer and denser pores in the network structure inside of wall, which hinder heat dissipation and lead to better insulation performance. Compared to the second stage, the first stage has a greater impact on the microstructure and properties of metal parts, as the solidification of the melt occurs during this stage, making honeycomb pattern more advantageous.

3.5 Evaluation and trial casting

According to the above investigations, the properties of shell moulds prepared with three infill patterns can be compared and evaluated. The flexural strength and shrinkage of the shell mould with a rectilinear pattern are the lowest, and the anisotropic shrinkage is significant. For the shell mould with a grid pattern, the porosity is the smallest. The shell mould with a honeycomb pattern exhibits the highest bending strength, porosity, and also demonstrates the best heat transfer ability and acceptable shrinkage. Taken together, the honeycomb pattern exhibits superior performance among the three infill patterns. High strength makes the shell mould less prone to damage. High porosity can improve permeability. A faster heat transfer is convince to obtain finer microstrcture and shorten

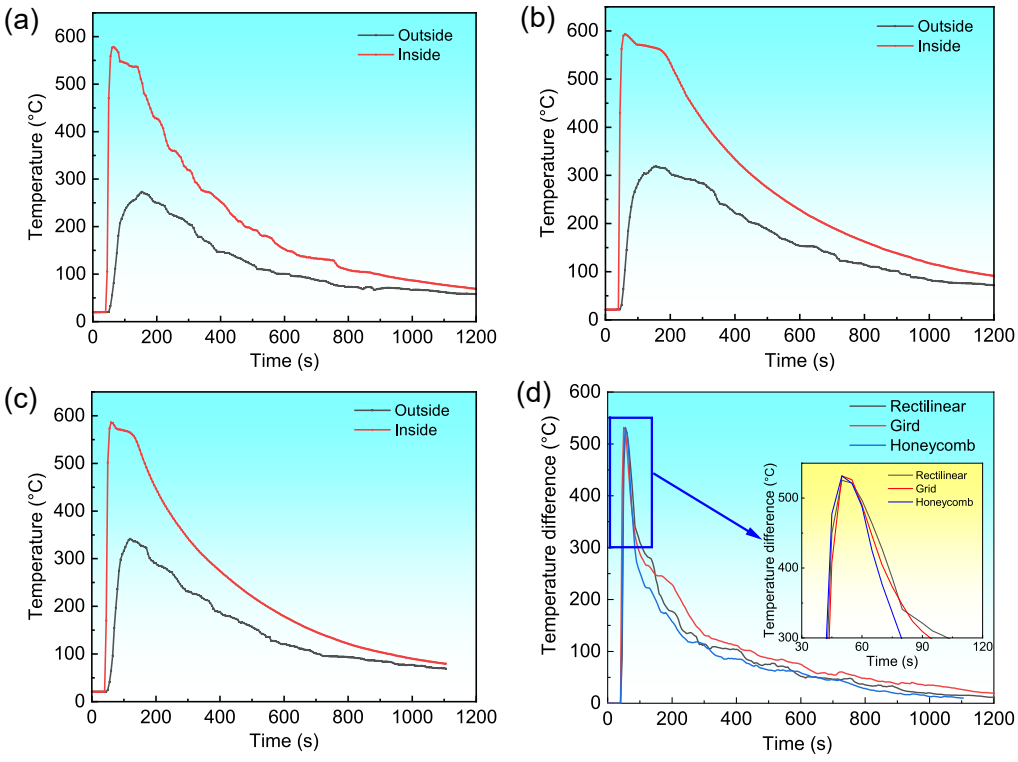

Fig. 10: Temperature curves after pouring (a–c) and temperature differences between inside and outside the shell moulds (d) with different filling patterns: (a) rectilinear pattern; (b) grid pattern; (c) honeycomb pattern

the production cycle. The shrinkage can be controlled within 2%, and the shrinkage in all directions is almost uniform.

A trial casting process was carried out using shell moulds with a honeycomb infill pattern prepared by the slurry extrusion-based additive manufacturing process. As shown in Fig. 11, two shell moulds were designed and fabricated, one forming the cavity of the casting, and the other forming a sprue (also serves as a riser) for the top pouring. Figure 11 also provides the details of the honeycomb pattern in the G-codes and printing process. The shell moulds were assembled after freeze-drying and sintering. The A356 aluminum alloy melt was poured into the mould cavity at 720 °C. After solidification and cooling, the shell mould was broken, and the casting was obtained. There is no obvious deformation or cracking of the shell moulds during the preparation and casting process, and the surface of the casting shows a layering appearance with additive manufacturing features.

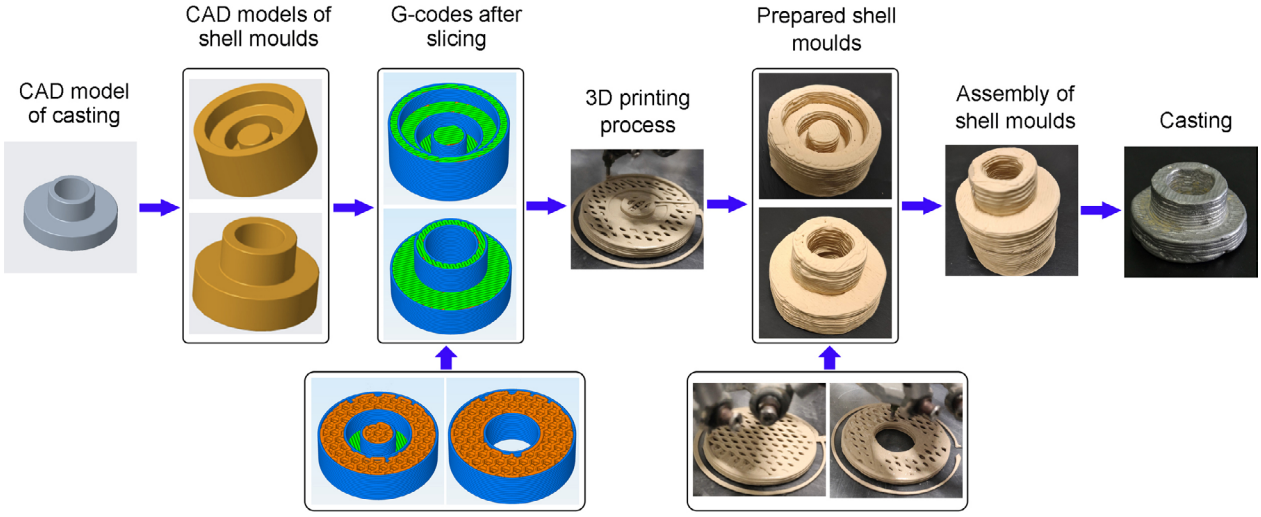

Fig. 11: Preparation and casting process of shell moulds with honeycomb pattern

4 Conclusion

The casting shell mould with a novel hierarchical porous structure, formed by the infill of the wall, can be fabricated by the slurry extrusion-based additive manufacturing process. The macropores formed through infills and the micropores among particles construct a hierarchical porous structure in the wall of shell mould. The different infill patterns lead to changes in the porous structure, thereby affecting the properties of the shell mould. The samples with the rectilinear pattern show the lowest bending strength, minimal shrinkage, and the worst heat-transfer ability. The porosity of samples with the grid pattern is the smallest. For the samples with the honeycomb pattern, their bending strength and porosity are the highest, and the heat-transfer ability is the best. Based on the comprehensive analysis, it is recommended to use the honeycomb infill pattern to prepare the shell mould. This research not only provides an alternative approach to preparing porous shell moulds with controllable porosities and properties but also highlights their potential applications as lightweight, high-strength shell moulds. Additionally, it reduces the usage of moulding materials, thereby contributing to sustainable development.

Acknowledgments

This work was financially supported by the National Natural Science Foundation of China (No. 52062029), the Key Science and Technology Project of Gansu Province (No. 18YF1GA064), and the Natural Science Foundation of Gansu Provence (No. 25JRRA094).

Conflict of interest

The authors declare that they have no known competing financial interests or personal relationships that could have appeared to influence the work reported in this paper.

References

[1] Shangguan H, Kang J, Deng C, et al. 3D-printed shell-truss sand mold for aluminum castings. Journal of Materials Processing Technology, 2017, 250: 247–253.
[2] Tang S, Yang L, Fan Z, et al. A review of additive manufacturing technology and its application to foundry in China. China Foundry, 2022, 18(4): 249–264.
[3] Kanyo J E, Schaffner S, Uwanyuze R S, et al. An overview of ceramic molds for investment casting of nickel superalloys. Journal of the European Ceramic Society, 2020, 40(15): 4955–4973.
[4] Bae C J, Kim D, Halloran J W. Mechanical and kinetic studies on the refractory fused silica of integrally cored ceramic mold fabricated by additive manufacturing. Journal of the European Ceramic Society, 2019, 39(2–3): 618–623.
[5] Shi Y, Zhang J, Wen S, et al. Additive manufacturing and foundry innovation. China Foundry, 2022, 18(4): 286–295.
[6] Oguntuyi S, Nyembwe K, Shongwe M, et al. Challenges and recent progress on the application of rapid sand casting for part production: A review. International Journal of Advanced Manufacturing Technology, 2023, 126(3–4): 891–906.

[7] Chen S, Wang C, Zheng W, et al. Effects of particle size distribution and sintering temperature on properties of alumina mold material prepared by stereolithography. Ceramics International, 2022, 48(5): 6069–6077.
[8] Gu Y, Duan W, Wang T, et al. Additive manufacturing of Al_2O_3 ceramic core with applicable microstructure and mechanical properties via digital light processing of high solid loading slurry. Ceramics International, 2023, 49(15): 25216–25224.
[9] Wen S, Shen Q, Wei Q, et al. Material optimization and post-processing of sand moulds manufactured by the selective laser sintering of binder-coated Al_2O_3 sands. Journal of Materials Processing Technology, 2015, 225: 93–102.
[10] Wei Q, Zhong J, Xu Z, et al. Microstructure evolution and mechanical properties of ceramic shell moulds for investment casting of turbine blades by selective laser sintering. Ceramics International, 2018, 44(11): 12088–12097.
[11] Rodríguez-González P, Fernández-Abia A I, Castro-Sastre M A, et al. Comparative study of aluminum alloy casting obtained by sand casting method and additive manufacturing technology. Procedia Manufacturing, 2019, 41: 682–689.
[12] Mitra S, Castro A R, Mansoria M E. On the rapid manufacturing process of functional 3D printed sand molds. Journal of Manufacturing Processes, 2019, 42(6): 202–212.
[13] Hao L, Tang D, Sun T, et al. Direct ink writing of mineral materials: A review. International Journal of Precision Engineering and Manufacturing-Green Technology, 2021, 8(2): 665–685.
[14] Maeng W Y and Lee H. Recent additive manufacturing methods categorized by characteristics of ceramic slurries for producing dual-scale porous ceramics. Biomedical Engineering Letters, 2020, 10(4): 481–492.
[15] Tang S, Yang L, Li G, et al. 3D printing of highly-loaded slurries via layered extrusion forming: Parameters optimization and control. Additive Manufacturing, 2019, 28: 546–553.
[16] Bratten A, Chen R, Rittenhouse J, et al. Improved additive manufacturing of silicon carbide parts via pressureless electric field-assisted sintering. International Journal of Applied Ceramics Technology, 2022, 19(5): 2480–2488.
[17] Zhang Z, Lin T, Shao H, et al. Preparation of 3DGP dense zirconia parts by two-step method: Staggered stacking method and printing wire deformation-science direct. Ceramics International, 2020, 46(5): 6491–6496.
[18] Shao H, He J, Lin T, et al. 3D gel-printing of hydroxyapatite scaffold for bone tissue engineering. Ceramics International, 2019, 45(1): 1163–1170.
[19] Yang L, Feng Q, Tang S, et al. Effect of $CaTiO_3$ on sintering properties of Y_2O_3-based ceramic shell via extrusion-based 3D printing for titanium alloy casting. Ceramics International, 2023, 49: 19338–19345.
[20] Choi H H, Kim E H, Kim B G, et al. Improvement of ceramic core strength by combining 3D printing technology and an organic-inorganic conversion process using dual polymers. Ceramics International, 2021, 47(12): 17644–17651.
[21] Xing Y, Zhou Y, Yan X, et al. Shell thickening for extrusion-based ceramics printing. Computers and Graphics, 2021, 97: 160–169.
[22] Zhu K, Yang D, Yu Z, et al. Additive manufacturing of SiO_2-Al_2O_3 refractory products via direct ink writing. Ceramics International, 2020, 46(17): 27254–27261.
[23] Hassan M R, Jeon H W, Kim G, et al. The effects of infill patterns and infill percentages on energy consumption in fused filament fabrication using CFR-PEEK. Rapid Prototyping Journal, 2021, 27(10): 1886–1889.
[24] Majd Y F, Tsuzuki M D G, and Barari A. Planning the infill patterns and the resulting density percentage error in additive manufacturing. Lecture Notes on Data Engineering and Communications Technologies, 2023, 146: 528–540.
[25] Fernandez-Vicente M, Calle W, Ferrandiz S, et al. Effect of infill parameters on tensile mechanical behavior in desktop 3D printing. 3D Printing and Additive Manufacturing, 2016, 3(3): 183–192.
[26] Agrawal A P, Kumar V, Kumar J, et al. An investigation of combined effect of infill pattern, density, and layer thickness on mechanical properties of 3D printed ABS by fused filament fabrication. Heliyon, 2023, 9(6): e16531.
[27] Mahatme C, Giri J, Chadge R, et al. Comparative analysis of different lattice topologies for cellular structure optimization in additive manufacturing. Materials Today: Proceedings, 2022, 62(3): 1591–1595.
[28] Man Y, Luo X, Xie Z, et al. Influence of 3D printed topological structure on lightweight mullite load bearing board in thermal environment. Advances in Materials Science and Engineering, 2020: 8340685.
[29] Hu K, Wang H, Lu K, et al. Fabrication of silica-based ceramic cores with internal lattice structures by stereolithography. China Foundry, 2022, 19(5): 369–379.
[30] Santoliquido O, Camerota F, Ortona A. The influence of topology on DLP 3D printing, debinding and sintering of ceramic periodic architectures designed to replace bulky components. Open Ceramics, 2021, 5: 100059.
[31] Zheng J, Hu X, Tang B, et al. Promoting sustainability in 3D printed sand casting through adaptive sand mold structures. Sustainable Materials and Technologies, 2024, 40: e00881.
[32] Xu J, Kang J, Hu Y, et al. Study on the mechanical properties of 3D-printed sand mold specimens with complex hollow structures. Materials, 2024, 17: 996.
[33] Liu H, Su G, Li Y. Effect of wall structure on the dimensional accuracy of shell mould prepared by slurry extrusion-based additive manufacturing process. Internaltional Journal of Cast Metals Research, 2022, 35(4): 102–110.
[34] Lu G, Chen Y, Yan Q, et al. Carbon-nylon hybrid fibers modified silica sol shell with enhanced flexural strength and heat transfer for investment casting. Journal of the European Ceramic Society, 2022, 42(8): 3624–3633.
[35] Venkat Y, Choudary K, Das D, et al. Ceramic shell moulds with zircon filler and colloidal silica binder for investment casting of shrouded low-pressure turbine blades. Ceramics International, 2020, 46(17): 26572–26580.
[36] Kanyo J, Schafföner S, Uwanyuze R, et al. An overview of ceramic molds for investment casting of nickel superalloys. Journal of the European Ceramic Society, 2020, 40(15): 4955–4973.
[37] Wang F, Li F, He B, et al. Microstructure and strength of needle coke modified ceramic casting molds. Ceramics International, 2014, 40(1), Part A: 479–486.
[38] Mao J, Liu H, Li Y. Influence of sintering temperature on the properties of precise casting shell prepared by additive manufacturing. Foundry Technology, 2020, 41(7): 607–611. (In Chinese)